

Disorder-Assisted Adiabaticity in Correlated Many-Particle Systems

Shang-Jie Liou¹ and Herbert F. Fotso¹

¹*Department of Physics, University at Buffalo SUNY, Buffalo, New York 14260, USA*

We investigate how disorder affects adiabaticity in an interacting quantum system by assessing its effect on the state of the system after an interaction modulation, or interaction “pulse”, whereby the interaction is changed from zero to a maximum value and then back to zero following a given time profile. We find that, independently of the disorder strength and pulse shapes (rectangular, triangular, and Gaussian), the pulse duration is negatively correlated with the change in total energy in the system. That is, the longer duration reduces the change in total energy for each protocol. Most importantly, across different considered pulse shapes, we find a robust negative correlation between the disorder strength and the change in total energy across the interaction pulse. Namely, increasing the disorder strength systematically suppresses the residual energy added to the system after the interaction pulse, indicating a more adiabatic response. These two effects, disorder-induced and duration-induced adiabaticity, are consistently observed across all three pulse shapes. Among the protocols, the triangular pulse yields the smallest change in total energy in the system over comparable conditions, demonstrating the most adiabatic response. In addition to the energy analysis, we also examine how disorder modifies the effective temperature change across the interaction pulse, to further establish a quantitative relation between disorder and the thermal response. Altogether, our results identify disorder as a key factor in both the energy and the temperature variation over the time-modulation of the interaction.

I. INTRODUCTION

Adiabaticity is a fundamental concept with applications in a variety of fields extending from thermodynamics[1–4], to quantum information processing[5–7], to quantum state preparation[8–11], and, more broadly, to many-body physics[12–14]. For quantum systems, adiabaticity is often related to the rate of change of the Hamiltonian and powers of the minimum energy separation between consecutive energy levels of the Hamiltonian[2, 15–19]. It has been extensively investigated for the preparation of quantum states of strongly correlated systems in optical lattices[8–10]. A general challenge for correlated many-particle systems is the difficulty of computing the energy gaps for large many-body systems. Also, given that disorder is typically a feature rather than the exception in realistic systems, it is important to understand its effect on the adiabaticity of many-particle systems.

In the present paper, we aim analyze the dynamics of a many-body system across a modulation of the interaction on a disordered system. Namely, we consider a system described by the Anderson-Hubbard model that features itinerant electrons on a lattice, a random site energy, and a Coulomb interaction for doubly occupied sites. We perform a time modulation of the interaction, or an interaction “pulse”, whereby the interaction starts off at zero and is increased to a maximum value before then being switched off again, according to a given pulse shape (rectangular, triangular, and Gaussian). We use our recently introduced Nonequilibrium DMFT+CPA[20–23] method that combines the nonequilibrium extensions of the dynamical mean field approximation (DMFT)[24–31] and that of the coherent potential approximation (CPA)[32–37], to appropriately treat the nonequilibrium dynamics of our interacting and disordered system. We probe adiabaticity through the residual total energy in the system after the interaction pulse.

Through these solutions, we find that independently of the disorder strength and pulse shape, longer pulse durations reduce the change in total energy in the system, as would be generally expected. Most importantly, across the different pulse shapes considered, we find a robust negative correlation between disorder strength and the residual energy added to the system after the interaction modulation. Namely, increasing the disorder strength systematically suppresses the change in total energy after the interaction is returned to zero, indicating a more adiabatic response of the system to the interaction pulse.

These two effects, disorder-induced and duration-induced adiabaticity, are consistently observed across all three protocol shapes. Among the pulse shapes considered, the triangular protocol displays the smallest change in total energy in the system under comparable conditions, demonstrating the most adiabatic response. In addition to the energy analysis, to establish a quantitative relation between disorder and the thermal response, we examine how disorder affects the effective temperature change during the interaction modulation process. Consistently with the change in total energy, the variation in temperature across the interaction pulse is reduced by both the pulse duration and the disorder strength. Taken altogether, our results identify disorder, protocol duration, and protocol shape as key factors governing both energy and temperature evolution during interaction modulation i.e. as control parameters for more adiabatic evolution.

The rest of the paper is structured as follows. In section II, we discuss our model and its solution with our nonequilibrium DMFT+CPA approach. In section III, we present our results before concluding with section IV.

II. MODEL AND METHODS

A. Model

We consider a disordered correlated electronic system described by the single-band Anderson–Hubbard model, initially in equilibrium at temperature $T = 1/\beta$. The Hamiltonian is

$$H = - \sum_{\langle ij \rangle, \sigma} t_{ij} \left(c_{i\sigma}^\dagger c_{j\sigma} + \text{H.c.} \right) + \sum_i U(t) n_{i\uparrow} n_{i\downarrow} + \sum_{i\sigma} (V_i - \mu) n_{i\sigma}. \quad (1)$$

Here, $t_{ij} = t_{\text{hop}}$ is the hopping amplitude between nearest-neighbor sites denoted by $\langle ij \rangle$, $U(t)$ is the on-site Coulomb interaction at time t , and V_i is the random on-site disorder potential. The operators $c_{i\sigma}^\dagger$ ($c_{i\sigma}$) create (annihilate) an electron of spin $\sigma = \uparrow, \downarrow$ at site i , and $n_{i\sigma} = c_{i\sigma}^\dagger c_{i\sigma}$ is the corresponding number operator. The chemical potential μ is set to $U/2$ to ensure half-filling. We work in units where $\hbar = e = c = 1$. The disorder potential V_i follows a uniform box probability distribution between $-W$ and $+W$, $P(V_i) = \frac{1}{2W} \Theta(W - |V_i|)$, where W characterizes the strength of the disorder. The problem is solved on the Bethe lattice in the limit of infinite coordination number $z \rightarrow \infty$, for which the hopping amplitude is rescaled as $t_{\text{hop}} = t^*/\sqrt{z}$. We choose $t^* = 0.25$ and we use the bandwidth $4t^* = 1$ as the unit of energy and time.

Under equilibrium conditions, the interaction $U(t)$ remains constant. In contrast, for the nonequilibrium scenarios of interest in the present paper, $U(t)$ varies in time according to a given profile. In this work, we examine three distinct "pulse" shapes — rectangular, triangular, and Gaussian — each characterized by the maximum amplitude U_{max} and designed such that $U(t) \rightarrow 0$ at sufficiently early and late times. The disorder potential $\{V_i\}$ remains constant throughout the evolution.

In the rectangular pulse case, the interaction is abruptly switched on from $U = 0$ to a finite value U_{max} for a fixed duration T_p , and then switched off again, following $U(t) = 0$ for $t < 0$, $U(t) = U_{\text{max}}$ for $0 \leq t < T_p$, and $U(t) = 0$ for $t \geq T_p$. This form allows us to analyze the response of the system to a sudden and finite-duration interaction pulse. On the other hand, the triangular pulse rises linearly from zero at $t = 0$ to U_{max} at time $t = t_0$ and symmetrically decays back to zero, with a total pulse width T_p , such that $U(t) = 0$ for $|t - t_0| > T_p/2$ and $U(t) = U_{\text{max}}(1 - |t - t_0|/(T_p/2))$ for $|t - t_0| \leq T_p/2$. The triangular pulse profile features smoother ramping and decay than the rectangular pulse. Finally, the Gaussian pulse varies continuously according to $U(t) = U_{\text{max}} \exp[-(t - t_0)^2/(2\sigma^2)]$, where t_0 is the pulse center (with $U(t_0) = U_{\text{max}}$) and σ denotes the standard deviation of the pulse. σ is chosen such that $U(0) = 0.01 U_{\text{max}}$, giving $\sigma = \sqrt{-t_0^2/[2 \ln(0.01)]}$; also, the pulse width is determined by $T_p = 2t_0$. These three time-dependent profiles of $U(t)$ represent different ways of modulating the interaction, allowing us to

investigate how the shape of the interaction strength influences the disordered system's ability to respond adiabatically. Each type of pulse starts and ends at zero interaction, meaning that the system returns to its initial non-interacting configuration. For these different pulse shapes, we will evaluate the residual energy, change in total energy, in the system after the pulse. We will also assess the temperature change due to the pulse.

B. Nonequilibrium DMFT+CPA

To study the nonequilibrium dynamics of the Anderson–Hubbard model, we employ our recently introduced method that combines the nonequilibrium extensions of the dynamical mean-field theory (DMFT) [24–26] and that of the coherent potential approximation (CPA) [32, 33] into a solution that we have called DMFT+CPA [20, 23]. The method is schematically summarized in Fig. 1. Both DMFT and CPA self-consistently reduce the many-body lattice problem to an effective single-impurity model that can be solved numerically. DMFT maps the entire lattice model with randomly distributed disorder potentials onto a set of disorder configurations defined on a single impurity site; we need to compute the impurity Green's function $G_{V_i}(t, t')$ for each V_i disorder configuration by solving the corresponding impurity problem. We then average over all configurations within the CPA framework to obtain $G_{\text{ave}}(t, t')$. This averaged Green's function $G_{\text{ave}}(t, t')$, known as the DMFT+CPA solution, incorporates the effects of both disorder and interactions, thus it characterizes the whole system. Note that the self-consistency loop between Fig. 1(b) and Fig. 1(c) is performed by updating the hybridization function $\Delta(t, t')$ until the convergence of $G_{\text{ave}}(t, t')$ is reached.

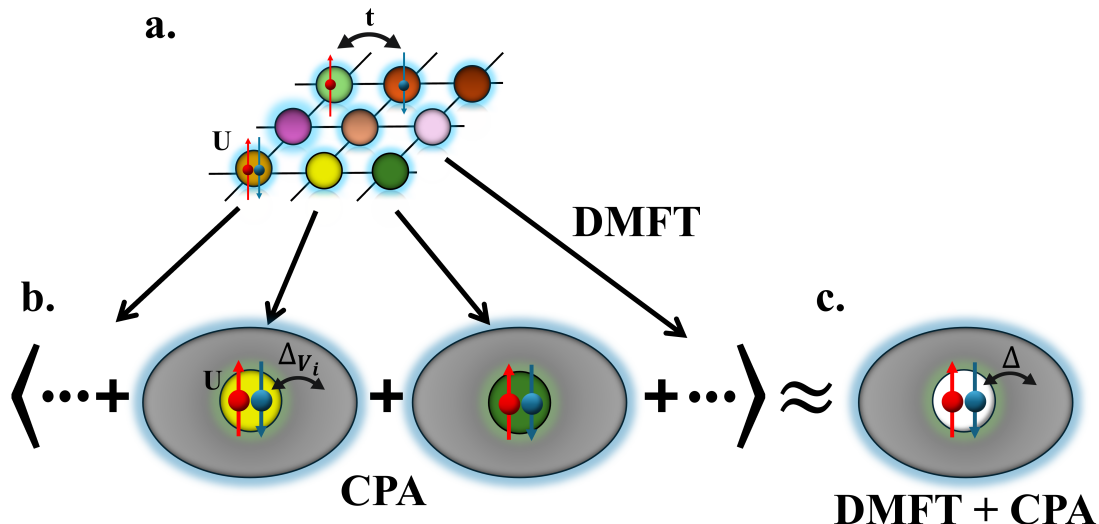


FIG. 1. Schematic illustration of the DMFT+CPA solution: (a) Anderson-Hubbard model, electrons can hop between the nearest neighboring lattice sites i and j with hopping amplitude t_{ij} , experience an on-site interaction energy U for doubly occupied sites, and are subject to random disorder potential V_i (shown as different colors in the figure). (b) Based on DMFT, the disordered lattice is mapped onto a set of disorder configurations on a single impurity site, whose Green's function is computed by coupling the impurity to an effective bath via a self-consistently determined hybridization function $\Delta(t, t')$. (c) Within the CPA framework, we average over all disorder configurations to obtain the averaged Green's function $G_{\text{ave}}(t, t')$, which constitutes the DMFT+CPA solution. The self-consistency loop between panels (b) and (c) is iterated until $G_{\text{ave}}(t, t')$ converges.

The formalism is constructed on the Kadanoff–Baym–Keldysh contour [38–44], which, due to the absence of Gell-Mann-Low theorem for the nonequilibrium problem, evolves the system from an initial time t_{\min} forward to t_{\max} , back to t_{\min} , and then downward along the imaginary time axis to $t_{\min} - i\beta$. In this work, the interaction strength $U(t)$ is explicitly turned on and then turned off according to the chosen pulse protocol, as illustrated schematically in Fig. 2.

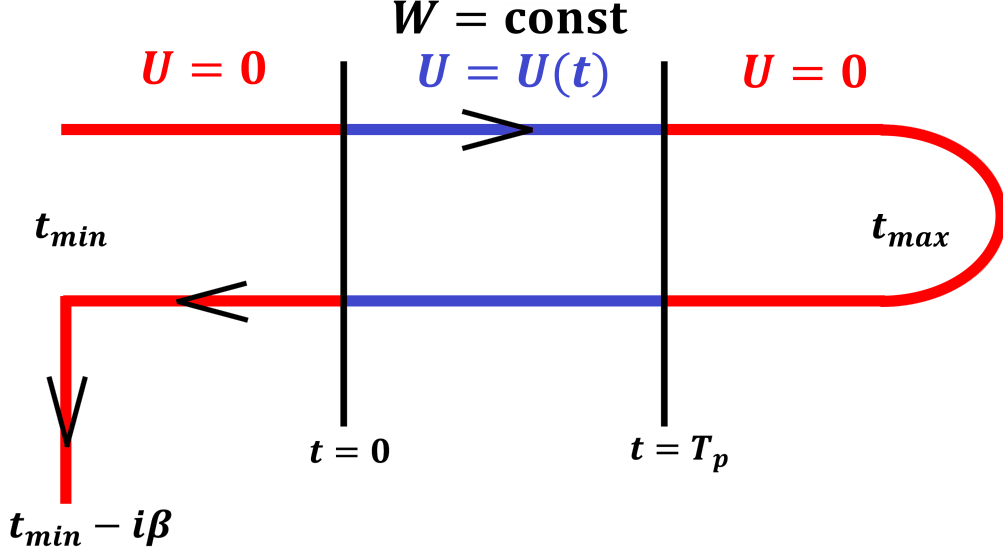


FIG. 2. The Kadanoff–Baym–Keldysh contour: the system is evolved from an initial time t_{\min} forward to t_{\max} , back to t_{\min} , and then downward along the imaginary time axis to $t_{\min} - i\beta$. The interaction pulse $U(t)$ starts at $t = 0$ and ends at $t = T_p$, where T_p denotes the pulse duration. The disorder strength W is kept constant throughout the evolution. The real and imaginary-time segments of the contour are discretized using step sizes Δt and $\Delta\tau$, respectively.

The central object of the formalism is the contour-ordered Green’s function

$$G_{ij,\sigma}(t, t') = -i\langle T_c c_{i\sigma}(t) c_{j\sigma}^\dagger(t') \rangle, \quad (2)$$

where T_c orders operators along the contour. From this quantity, other real-time Green’s functions can be extracted, including the lesser $G^<(t, t')$, greater $G^>(t, t')$, and retarded $G^R(t, t')$ functions. The contour-ordered Green’s function defined on the Kadanoff–Baym–Keldysh contour provides a unified description of equilibrium and nonequilibrium dynamics. Depending on the positions of the time arguments on the contour branches, different real-time components can be obtained. In particular, the lesser and greater Green’s functions describe particle correlations and occupation properties, while the retarded Green’s function characterizes the causal response of the system. These components follow from projecting the contour-ordered Green’s function onto the corresponding segments of the contour and are related through standard analytic relations within the nonequilibrium Green’s function formalism. Detailed description of this framework can be found in [42–44]. Within the DMFT+CPA framework, the lattice problem is mapped onto a single impurity problem embedded in a self-consistently determined medium characterized by the hybridization function $\Delta(t, t')$ [23]. For a given disorder configuration, the noninteracting impurity Green’s function is

$$\mathcal{G}_{V_i}(t, t') = [(i\partial_t + \mu - V_i)\delta_c - \Delta]^{-1}(t, t'), \quad (3)$$

and the interacting impurity Green’s function is obtained from the Dyson equation,

$$G_{V_i}(t, t') = [(\mathcal{G}_{V_i})^{-1} - \Sigma_{V_i}]^{-1}(t, t'), \quad (4)$$

where $\Sigma_{V_i}(t, t')$ is the self-energy for the impurity with on-site disorder V_i . We employ second-order perturbation theory as the impurity solver. Resulting in the self-energy:

$$\Sigma_{V_i}(t, t') = -U(t)U(t') G_{V_i}(t, t')^2 G_{V_i}(t', t). \quad (5)$$

The notation $\langle \dots \rangle_{\{V\}}$ indicates an average over all possible disorder configurations. Following Eq. 4, the disorder-averaged Green's function is obtained by

$$G_{\text{ave}}(t, t') = \langle G_{V_i}(t, t') \rangle_{\{V\}}. \quad (6)$$

On the infinite-dimensional Bethe lattice, the hybridization function is updated via

$$\Delta(t, t') = t^{*2} G_{\text{ave}}(t, t'). \quad (7)$$

This defines the self-consistency loop: starting from an initial guess of $\Delta(t, t')$, we compute $G_{V_i}^0$, evaluate Σ_{V_i} and G_{V_i} for each disorder configuration, average to obtain G_{ave} , update Δ , and iterate until convergence of G_{ave} is reached within a prescribed tolerance.

In the present work, the lattice is taken to be an infinite-dimensional Bethe lattice, which leads to the compact form of the hybridization (7), and simplifies the DMFT self-consistency loop described above. While the Bethe lattice does not correspond to a specific crystal structure, it is widely used in DMFT studies because it captures the essential feature that the electronic self-energy remains local in the infinite dimensional lattice. Although quantitative details may depend on the lattice geometry and dimensionality, many qualitative features of strongly correlated systems obtained within DMFT are known to remain robust when comparing different lattice structures, especially for lattices with high coordination numbers. Therefore, the Bethe lattice provides a convenient framework for studying the interplay of interactions, disorder, and nonequilibrium dynamics.

The nonequilibrium DMFT+CPA framework establishes an effective medium that simultaneously captures the effects of both electron–electron interaction and disorder in the nonequilibrium regime. The applicability of the DMFT+CPA framework relies on the locality of the self-energy and on the effective-medium treatment of disorder. Dynamical mean-field theory becomes exact in the limit of infinite lattice coordination number, where the self-energy is purely local and nonlocal spatial correlations are neglected while local dynamical correlations are fully retained. Within this framework, disorder is incorporated through the coherent potential approximation by averaging over impurity problems corresponding to different local disorder potentials V_i , yielding a disorder-averaged Green's function that defines the effective medium self-consistently. This procedure is known to appropriately capture the effect of weak to moderate disorder strengths. In the present work, the Anderson–Hubbard model is considered on an infinite-dimensional Bethe lattice, for which the DMFT self-consistency condition is valid. Therefore, the combined DMFT+CPA approach provides a consistent description of the nonequilibrium dynamics of interacting electrons in the presence of site-energy disorder.

The Green's function on the Kadanoff–Baym–Keldysh contour are discretized into $(2N_t + N_\tau)$ time points, where N_t denotes the number of steps along each branch of the real-time contour and N_τ corresponds to the imaginary-time branch. The step sizes are given by $\Delta t = (t_{\text{max}} - t_{\text{min}})/N_t$ for real time and $\Delta\tau = \beta/N_\tau$ for imaginary time. In this work, we use $t_{\text{min}} = -5$, $t_{\text{max}} = 20$, and an initial inverse temperature $\beta_{\text{initial}} = 15$, with a typical choice of $N_\tau = 100$. Contour-ordered quantities such as $G(t, t')$ are represented as square complex matrices G_{ij} of dimension $(2N_t + N_\tau) \times (2N_t + N_\tau)$, where convolutions become matrix multiplications and continuous inverses are replaced by discrete matrix inverses. To analyze the nonequilibrium dynamics, we employ Wigner coordinates $(T_{\text{ave}}, t_{\text{rel}})$, where T_{ave} represents the average (or effective) time of the system, and Fourier transforms with respect to t_{rel} provide access to frequency-domain information. Observables such as the distribution function and energy are computed on three different real-time grids, with typical values of $N_t \sim 1000$, and are subsequently extrapolated to the continuum limit $\Delta t \rightarrow 0$ using quadratic Lagrange interpolation.

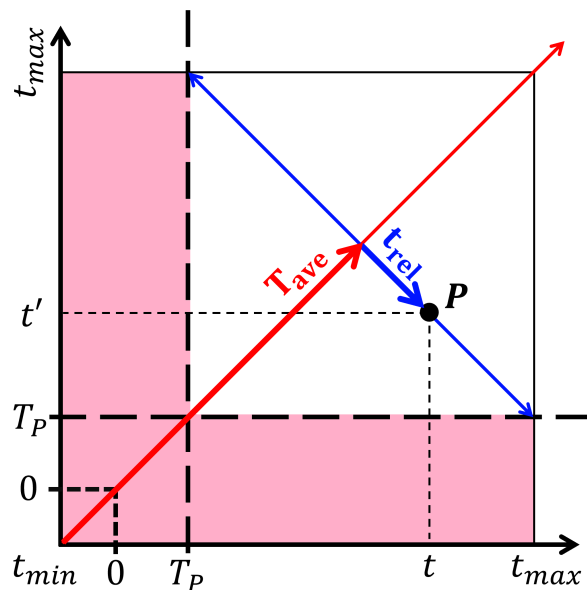


FIG. 3. Illustration of the relation between the contour-time coordinates (t, t') and the Wigner coordinates $(T_{\text{ave}}, t_{\text{rel}})$ for a point P in the two-time space, where T_p denotes the end of the pulse. The pink region indicates the portion of the data that needs to be truncated when evaluating physical quantities in frequency domain after the pulse.

C. Effective temperature

For the calculation of the effective temperature, the method introduced in [20] is not suitable for the present system. That approach relies on using the equilibrium energy-versus-temperature data to infer the effective temperature of a nonequilibrium system once it has reached its long-time state. However, in the present case, the system is altered by the interaction pulse and is not allowed to equilibrate through scattering processes due to the interaction. As a result, the potential energy remains unchanged while the kinetic and total energies vary. Because of this, the final state cannot be matched with an equilibrium state simply by equating the total energy to the equilibrium energy-temperature data curve. Therefore, we instead use the fluctuation-dissipation theorem to analyze the final state after the interaction pulse and deduce an effective temperature of the long-time state of the system.

First, because we need to analyze the Green's function in the frequency domain, the time coordinates are transformed from (t, t') to the Wigner coordinates $(T_{\text{ave}}, t_{\text{rel}})$. This transformation, illustrated schematically in Fig. 3, introduces T_{ave} , typically interpreted as the effective time of the system, and t_{rel} , the variable with respect to which Fourier transforms are performed to obtain frequency-space quantities. A Fourier transform of the retarded Green's function is followed by

$$G^R(T_{\text{ave}}, \omega) = \int dt_{\text{rel}} e^{i\omega t_{\text{rel}}} G^R(T_{\text{ave}}, t_{\text{rel}}), \quad (8)$$

To obtain the effective temperature, or its inverse β_{final} , after the pulse, we apply the nonequilibrium formalism described above to the system in time. The density of states is obtained from the nonequilibrium retarded Green's function $G^R(T_{\text{ave}}, \omega)$:

$$\rho(\omega) = -\frac{1}{\pi} \text{Im}[G^R(T_{\text{ave}}, \omega)]. \quad (9)$$

In an equilibrium system, the result of this operation is, in principle, independent of T_{ave} , which is not the case for the nonequilibrium system. The value of T_{ave} must be carefully chosen such that the available range of t_{rel} provides the most reliable numerical evaluation for the Fourier transform (typically taken near the midpoint of the average-time axis). In addition, because the data prior to the end of the pulse are contaminated due to including times t and t' where one is in the pulse and the other after the pulse, the pink region in Fig. 3 must be truncated. To summarize, we choose T_{ave} at the midpoint of the remaining average-time interval after the truncation, which is the white area in Fig. 3. Based on the fluctuation–dissipation theorem, a thermalized system satisfies

$$G^<(\omega) = -2i F(\omega) \text{Im}G^R(\omega), \quad (10)$$

where $F(\omega)$ denotes the distribution function. The effective temperature is obtained by fitting the system’s distribution function to a Fermi–Dirac $F(\omega) = \frac{1}{1+\exp(\beta\omega)}$ with β as a free parameter, which is extracted from the fit over a small frequency window around the Fermi energy $-0.1 < \omega < 0.1$. Because the truncation limits the accessible range of t_{rel} , an extension of the time range may be necessary. This consideration will be examined in the Results section.

III. RESULTS

A. Change in energy for different interaction pulse shapes and disorder

We study the nonequilibrium dynamics induced by an interaction pulse, during which the interaction strength $U(t)$ is switched on and subsequently turned off, starting and ending at zero following a given time-dependent profile. We compute kinetic, potential, and total energies as functions of time [45]. From the expression of the kinetic energy per lattice site as

$$E_{\text{kin}}(t) = \frac{1}{N} \sum_{k,\sigma} \varepsilon_k \left\langle c_{k,\sigma}^\dagger(t) c_{k,\sigma}(t) \right\rangle, \quad (11)$$

where N denotes the number of lattice sites, k the momentum vector, and ε_k is the band dispersion, it can therefore be re-expressed as

$$E_{\text{kin}}(t) = 2 \int d\varepsilon \rho(\varepsilon) \varepsilon G^<(t, t), \quad (12)$$

where ε is the band energy. The potential energy is obtained from the expression:

$$E_{\text{pot}}(t) = [G_{\text{ave}} * \Sigma_{\text{ave}}]^<(t, t) + \frac{U(t)}{4}. \quad (13)$$

The total energy can be obtained directly by summing up the kinetic and potential energies.

We track the variation of these different types of energy across the interaction modulation for different profiles and as a function of disorder. Figures (4)–(6) display the time evolution, shown in the (a) panels, of the potential (blue), kinetic (red), and total (black) energies for rectangular, Gaussian, and triangular pulses respectively, for disorder strengths $W = 0.5t^*$ (solid line), $W = 1.5t^*$ (dashed line), $W = 2t^*$ (dotted line). After the interaction returns to zero, the potential energy also vanishes and returns to its initial value. However, the kinetic energy after the pulse is different from its initial value, leading to a similar behavior of the total energy. The (b) panels of the figures show the change in total energy across the interaction pulse as a function of the disorder strength. Across all pulse shapes, we see that the change in total energy is suppressed by an increased disorder strength.

Fig. 7 shows a comparison in the time evolution of the energies for different pulse shapes, with the same area under the curve, for disorder strength $W/t^* = 2$ in panel (a). In panel (b), it presents

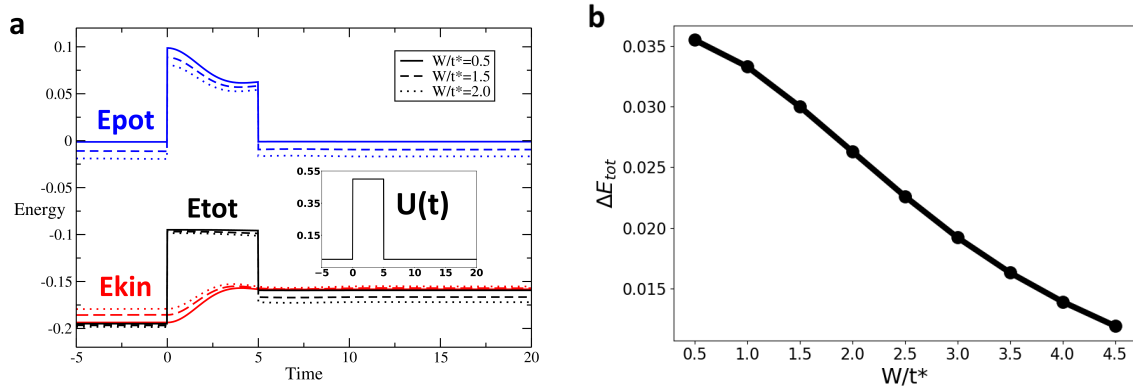


FIG. 4. For the rectangular pulse interaction ($U_{\max}/t^* = 2$, pulse width $T_p=5$), the change in total energy ΔE_{tot} systematically decreases as the disorder strength W increases, indicating that disorder promotes adiabaticity for this sharp on-off driving: (a) Energy as function of time for rectangular pulse interaction with $U_{\max}/t^* = 2$, and pulse width $T_p = 5$ for $W/t^* = 0.5, 1.5, 2$. The blue, red, and black lines represent the potential, kinetic, and total energy, respectively. (b) ΔE_{tot} vs W for Rectangular Pulse with $U_{\max}/t^* = 2$, and pulse width $T_p = 5$. ΔE_{tot} is defined as $E_{tot}(t_{\max}) - E_{tot}(t_{\min})$

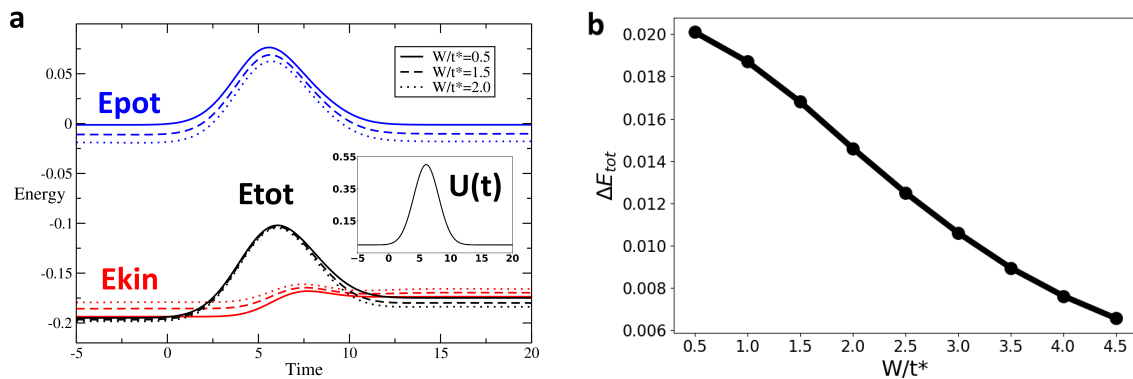


FIG. 5. For the Gaussian pulse interaction ($U_{\max}/t^*=2$, pulse width $T_p=12.14$), ΔE_{tot} again decreases with increasing disorder. In this smoothly varying protocol, disorder enhances the adiabatic response in agreement with the rectangular and triangular cases: (a) Energy as function of time for Gaussian pulse interaction with $U_{\max}/t^*=2$, and pulse width $T_p=12.14$ for $W/t^*=0.5, 1.5, 2$. (b) ΔE_{tot} vs W for gaussian Pulse with $U_{\max}/t^*=2$, and pulse width $T_p=12.14$.

the change in total energy as a function of disorder strength for the rectangular pulse (black), for the Gaussian pulse (red) and for the triangular pulse (blue) as a function of the disorder strength. We observe that, for all pulse shapes, increased disorder suppresses the change in total energy, thus showing a more adiabatic response. Moreover, the triangular pulse protocol is seen to yield the smallest ΔE_{tot} .

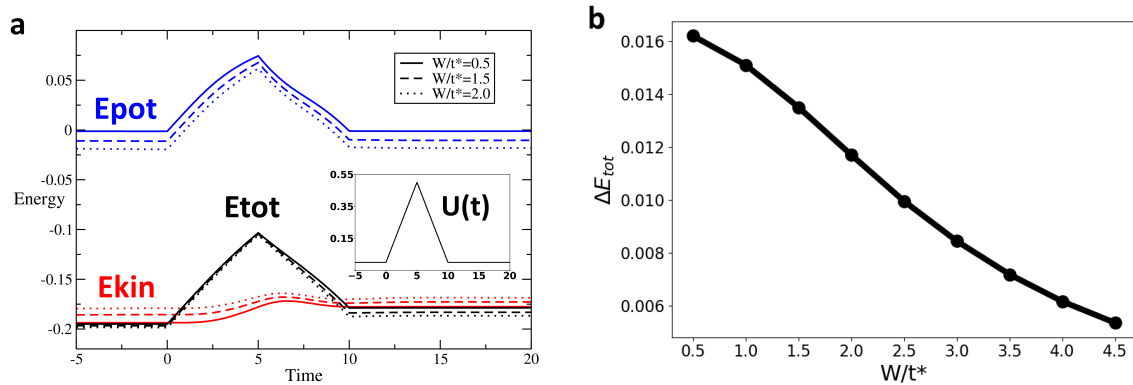


FIG. 6. For the triangular pulse interaction ($U_{\max}/t^* = 2$, pulse width $T_p = 10$), a similar decrease of ΔE_{tot} with increasing disorder is observed, showing that disorder also enhances adiabaticity in a gradual ramping protocol: (a) Energy as function of time for triangular pulse interaction with $U_{\max}/t^* = 2$, and pulse width $T_p = 10$ for $W/t^* = 0.5, 1.5, 2$. (b) ΔE_{tot} vs W for Triangular Pulse with $U_{\max}/t^* = 2$, and pulse width $T_p = 10$.

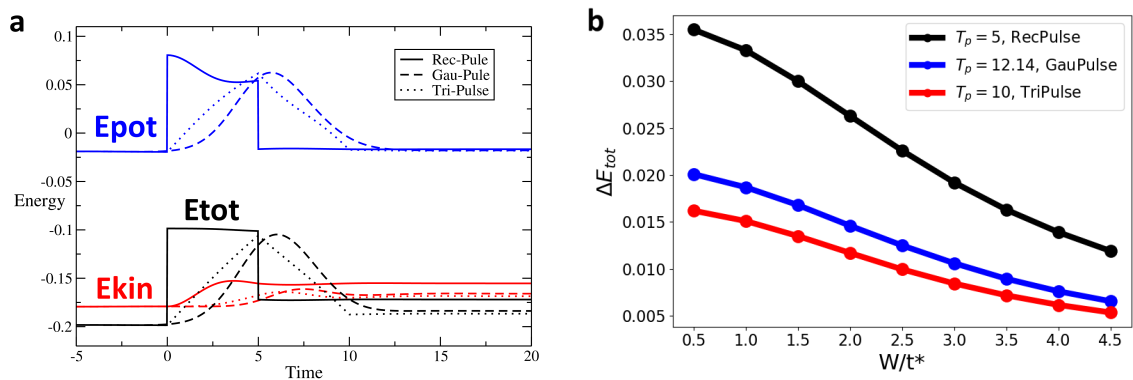


FIG. 7. For the rectangular, triangular and gaussian pulses interaction ($U_{\max}/t^*=2$, equal area), ΔE_{tot} always decreases with increasing disorder strength W . This shows that disorder enhances the adiabaticity of the process regardless of the type of interaction pulse applied: (a) Energy as function of time for rectangular, triangular and gaussian pulse interaction with $U_{\max}/t^*=2$ and equal area (different T_p) at $W/t^*=2$. (b) ΔE_{tot} vs W/t^* for three pulse types with $U_{\max}/t^*=2$ and equal area.

B. Change in energy for different pulse durations and disorder

Figures (8), (9) and (10) show in the (a) panels, respectively for the rectangular, the triangular and the Gaussian pulse respectively, the time evolution of the potential energy (blue), kinetic energy (red) and total energy (black) for different pulse durations T_p . The (b) panels of the figures show the change in total energy, ΔE_{tot} , across the interaction pulse as a function of the disorder strength for different pulse durations. While we see that pulse duration has the weakest effect on ΔE_{tot} for the rectangular pulse, a broader pulse leads to a smaller ΔE_{tot} . Most importantly, we observe that increased disorder strength has a stronger effect in producing a more adiabatic response than the pulse duration, eventually overwhelming the effect of the pulse duration for moderate to strong disorder strength.

The change in the total energy following the interaction modulation reflects the degree of nona-

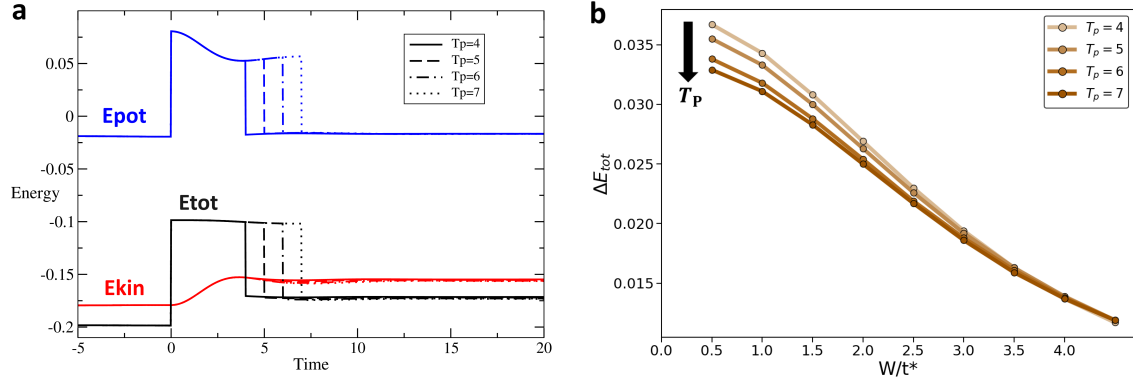


FIG. 8. For the rectangular interaction pulse ($U_{max}/t^*=2$, $W/t^*=2$), ΔE_{tot} decreases as the pulse period T_p increases, indicating that a longer period promotes adiabaticity in the rectangular pulse interaction: (a) Energy as function of time for rectangular pulse interaction with $U_{max}/t^*=2$ and $W/t^*=2$ for pulse width $T_p=4, 5, 6, 7$. The blue, red, and black lines represent the potential, kinetic, and total energy, respectively. (b) ΔE_{tot} vs W for rectangular pulse, colors transition from light brown to dark brown corresponding to pulse width $T_p=4, 5, 6, 7$ respectively.

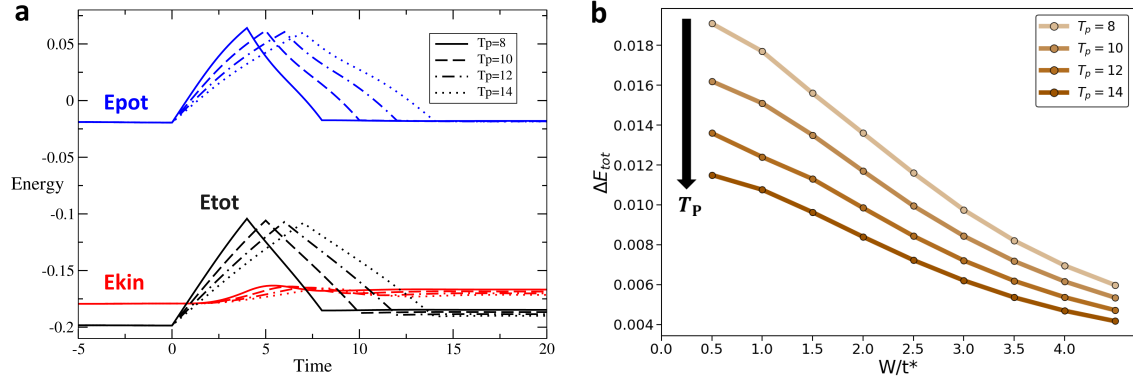


FIG. 9. For the Triangular interaction pulse ($U_{max}/t^*=2$, $W/t^*=1.0$), ΔE_{tot} decreases with increasing pulse period T_p , showing that longer pulse width enhance adiabaticity for the triangular driving protocol: (a) Energy as a function of time for triangular pulse interaction with $U_{max}/t^*=2$ and $W/t^*=1.0$ for pulse width $T_p=8, 10, 12, 14$. (b) ΔE_{tot} vs W for triangular pulse, colors transition from light brown to dark brown corresponding to pulse width $T_p=8, 10, 12, 14$ respectively.

diabaticity across the pulse. When the interaction strength is varied in time, the system absorbs energy as the modulation drives transitions between many-body states. The magnitude of this energy increase depends on the rate of interaction change and this rate varies with the pulse shape. The change of the interaction is instantaneously tied to the potential energy thus the change in potential energy immediately vanishes when the interaction is returned to zero. However, the kinetic energy is dynamically adjusted and would eventually settled into a steady state value if the system were allowed to equilibrate over a long time with a finite interaction strength. Disorder further modifies this behavior by suppressing coherent electron motion and reducing the ability of the system to absorb energy from the interaction modulation. As the disorder strength increases, it limits the generation of nonequilibrium excitations, the kinetic energy change across the pulse is reduced and leads to a smaller change in the total energy. These combined effects explain

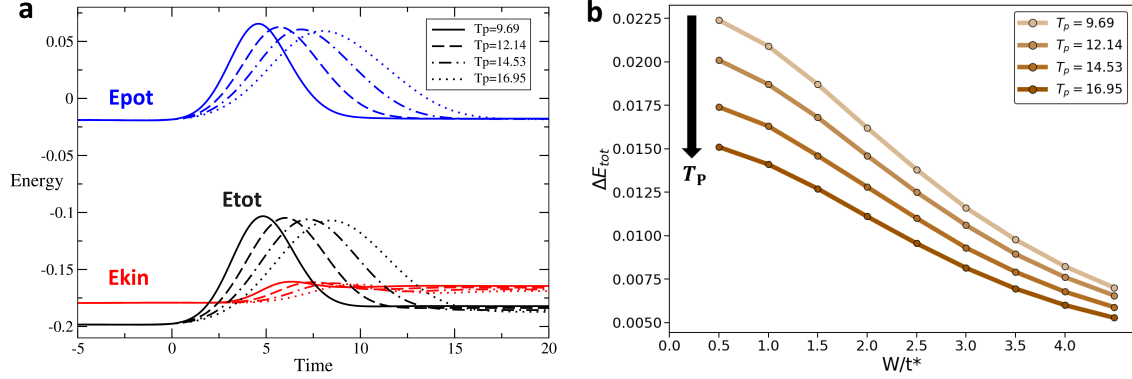


FIG. 10. For the gaussian interaction pulse ($U_{\text{max}}/t^*=2$, $W/t^*=2$), ΔE_{tot} also decreases as the width T_p grows, demonstrating that extended periods improve adiabaticity in the gaussian pulse case: (a) Energy as a function of time for gaussian pulse interaction with $U_{\text{max}}/t^*=2$ and $W/t^*=2$ for width $T_p = 9.69, 12.14, 14.53, 16.95$. (b) ΔE_{tot} vs W for gaussian pulse, colors transition from light brown to dark brown corresponding to pulse widths $T_p = 9.69, 12.14, 14.53, 16.95$ respectively.

the trends observed in our numerical results for different pulse protocols, durations, and disorder strengths. Overall, pulse protocols that keep the interaction near its maximum value for longer intervals tend to produce larger values of ΔE_{tot} and stronger nonadiabatic effects. The pulse duration also plays an important role: longer pulses allow the system to adjust more gradually to the time-dependent interaction through a redistribution of the additional potential energy into kinetic energy and therefore approach a more adiabatic evolution, resulting in smaller energy absorption when the interaction is returned to zero.

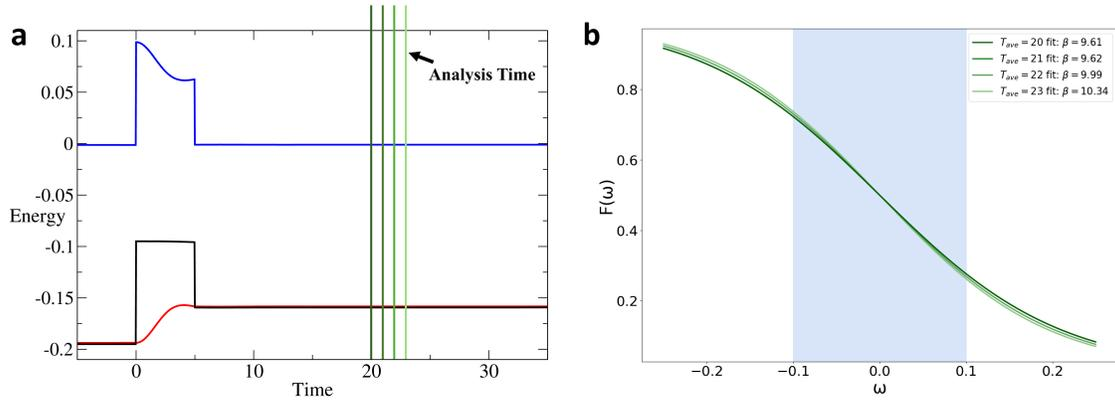


FIG. 11. Effective temperature analysis for the rectangular pulse interaction with $U_{\text{max}}/t^*=2$, pulse width $T_p = 5$, $\beta_{\text{initial}} = 15$ and $W/t^* = 0.5$. the time scale range is from -5 to 35 (a) The green lines represent the analysis time T_{ave} . (b) Post-relaxation $F(\omega)$ for $T_{\text{ave}} = 20$ (midpoint of the residual interval) and slightly later T_{ave} .

C. Effective final temperature vs. U for Different Pulse shape and W

Finally, we investigate the evolution of the effective temperature in the system under the time modulation of the interaction. As previously noted, the numerical analysis of the effective temperature after the pulse requires a careful choice of the average time T_{ave} and a sufficient range of relative time t_{rel} to perform a reliable Fourier transform for the application of the fluctuation dissipation theorem. Therefore, care is taken to appropriately choose the parameters for the extraction of the effective temperature of the system.

As shown in Fig.(11), A distribution function can be obtained after the interaction pulse with little dependence on the precise T_{ave} value. From this distribution function, a fit of the Fermi-Dirac distribution near the Fermi energy allows us to obtain the effective final temperature or its inverse. Fig. (12) shows the inverse of the effective temperature as a function of U_{max} for different disorder strengths. This analysis is in general agreement with that of the change in total energy. The triangular pulse produces the smallest variation in temperature, indicating a more adiabatic response compared to the other pulse shapes. Moreover, stronger disorder promotes more adiabatic behavior across all pulse shapes.

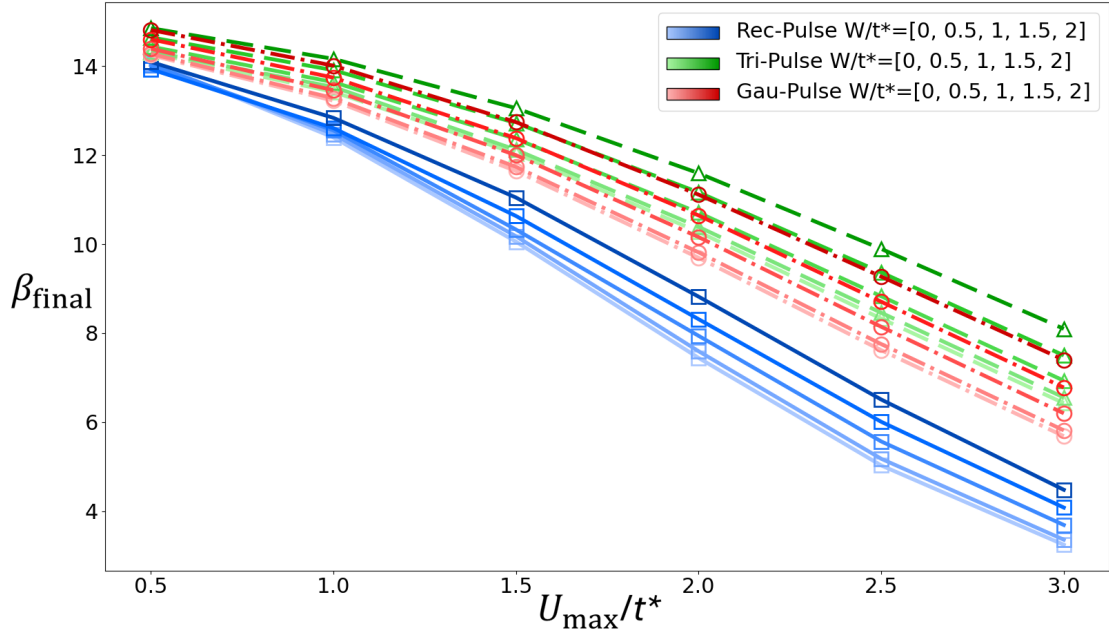


FIG. 12. Inverse of the final effective temperature β_{final} as a function of interaction strength U/t^* is shown for different pulse shapes and disorder strengths W ; the temperature before the pulse is $\beta_{\text{initial}} = 15$. The data for rectangular, triangular, and Gaussian pulses are plotted in blue, green, and red, respectively. For each pulse shape, the color intensity varies from light to dark corresponding to $W/t^* = 0.0, 0.5, 1.0, 1.5, 2.0$.

IV. CONCLUSIONS

We have used the nonequilibrium DMFT+CPA[20–23] solution to appropriately treat the nonequilibrium dynamics of an interaction disordered system across an interaction pulse, whereby the interaction starts off at zero and is increased to a maximum value before then being switched off again, according to a given pulse shape (rectangular, triangular, and Gaussian). We probe

adiabaticity through the residual total energy in the system or the variation of the effective temperature after the interaction pulse. Through these solutions, we find that independently of the disorder strength and pulse shape, longer pulse durations reduce the change in total energy in the system, as would be generally expected. Most importantly, across the different pulse shapes considered, we find a robust negative correlation between disorder strength and the change in total energy across the interaction modulation. Namely, increasing the disorder strength systematically suppresses the change in total energy after the interaction is returned to zero, indicating a more adiabatic response of the system to the interaction pulse. These two effects, disorder-induced and duration-induced adiabaticity, are consistently observed across all three protocol shapes. Among the pulse shapes considered, the triangular protocol displays the smallest change in total energy in the system under comparable conditions, demonstrating the most adiabatic response. Although the different pulse protocols are chosen to have the same total interaction area $\int U(t) dt$, they modify the interaction strength at different rates in time. In particular, the square pulse maintains the maximum interaction strength over an extended plateau, while the Gaussian pulse, although smooth, still spends a significant portion of the evolution near its peak value depending on the pulse width. By contrast, the triangular pulse reaches the maximum interaction only instantaneously and otherwise increases/decreases the interaction with a uniform rate between zero and the maximum value. Since the nonequilibrium response becomes stronger when the interaction strength is large, the longer time spent near U_{\max} in the square and Gaussian protocols leads to larger energy absorption when the interaction is returned to zero. The triangular pulse therefore produces the smallest increase in the total energy and thus, the most adiabatic response. This observation suggests that in addition to pulse duration, pulse protocols minimizing the time spent near the maximum interaction strength may provide a useful avenue for designing more optimal adiabatic driving schemes. Altogether, our results identify disorder, protocol duration, and protocol shape as key factors governing both energy and temperature evolution during interaction modulation i.e. as control parameters for more adiabatic evolution.

ACKNOWLEDGMENTS

This work was supported by the U.S. Department of Energy, Office of Science, Basic Energy Sciences, under Award #DE-SC0024139. We thank V. Oganesyan for useful discussions.

REFERENCES

-
- [1] D. Guéry-Odelin, A. Ruschhaupt, A. Kiely, E. Torrontegui, S. Martínez-Garaot, and J. G. Muga, “Shortcuts to adiabaticity: Concepts, methods, and applications,” *Rev. Mod. Phys.* **91**, 045001 (2019).
 - [2] M. Born and V. Fock, “Proof of the adiabatic theorem,” *Z. Phys.* **51**, 165–180 (1928).
 - [3] M. Herrera, R. M. Serra, and I. D’Amico, “Nonequilibrium thermodynamics of quantum systems with local control,” *Sci. Rep.* **7**, 4655 (2017).
 - [4] A. Skelt, K. Zawadzki, and I. D’Amico, “Quantum speed limits in driven open systems,” *Phys. Rev. Lett.* **127**, 030602 (2021).
 - [5] M. A. Nielsen and I. L. Chuang, *Quantum Computation and Quantum Information* (Cambridge University Press, Cambridge, 2000), doi:10.1017/CBO9780511976667.
 - [6] E. Farhi, J. Goldstone, and S. Gutmann, “Quantum adiabatic evolution algorithms with different paths,” arXiv:quant-ph/0208135 (2002).
 - [7] T. Albash and D. A. Lidar, “Adiabatic quantum computation,” *Rev. Mod. Phys.* **90**, 015002 (2018).

- [8] Anders S. Sørensen, Ehud Altman, Michael Gullans, J. V. Porto, Mikhail D. Lukin, and Eugene Demler, “Adiabatic preparation of many-body states in optical lattices,” *Phys. Rev. A* **81**, 061603(R) (2010).
- [9] I. Bloch, J. Dalibard, and W. Zwerger, “Many-body physics with ultracold gases,” *Rev. Mod. Phys.* **80**, 885 (2008).
- [10] J. J. García-Ripoll, M. A. Martin-Delgado, and J. I. Cirac, “Implementation of spin Hamiltonians in optical lattices,” *Phys. Rev. Lett.* **93**, 250405 (2004).
- [11] E. Farhi, J. Goldstone, and S. Gutmann, “Quantum adiabatic evolution algorithms with different paths,” arXiv:quant-ph/0208135 (2002).
- [12] H. Saberi, T. Opatrný, K. Mølmer, and A. del Campo, “Adiabatic tracking of quantum many-body dynamics,” *Phys. Rev. A* **90**, 060301(R) (2014).
- [13] L. Dupays, A. del Campo, and B. Dóra, “Slow approach to adiabaticity in many-body non-Hermitian systems: The Hatano–Nelson model,” *Phys. Rev. B* **111**, 045130 (2025).
- [14] M. Gell-Mann and F. Low, “Bound states in quantum field theory,” *Phys. Rev.* **84**, 350–354 (1951).
- [15] J. E. Avron and A. Elgart, “Adiabatic theorem without a gap condition,” *Commun. Math. Phys.* **203**, 445–463 (1999).
- [16] K.-P. Marzlin and B. C. Sanders, “Inconsistency in the application of the adiabatic theorem,” *Phys. Rev. Lett.* **93**, 160408 (2004).
- [17] D. M. Tong, K. Singh, L. C. Kwek, and C. H. Oh, “Quantitative conditions do not guarantee the validity of the adiabatic approximation,” *Phys. Rev. Lett.* **95**, 110407 (2005).
- [18] J. Ortigoso, “Note on the adiabatic approximation,” *Phys. Rev. A* **86**, 032121 (2012).
- [19] M. Born and R. Oppenheimer, “Zur Quantentheorie der Molekeln,” *Ann. Phys.* **389**, 457–484 (1927).
- [20] A. Abuelmaged, E. Dohner, S.-J. Liou, and H. F. Fotso, “Nonequilibrium dynamics of a disordered binary alloy,” *Phys. Rev. B* **112**, 134308 (2025).
- [21] E. Dohner, H. Terletska, and H. F. Fotso, “Thermalization of a disordered interacting system under an interaction quench,” *Phys. Rev. B* **108**, 144202 (2023).
- [22] C. Rangi, H. F. Fotso, H. Terletska, J. Moreno, and K.-M. Tam, “Disorder-enhanced thermalization in interacting many-particle systems,” *Phys. Rev. B* **111**, L161122 (2025).
- [23] E. Dohner, H. Terletska, K.-M. Tam, J. Moreno, and H. F. Fotso, “Nonequilibrium DMFT+CPA for correlated disordered systems,” *Phys. Rev. B* **106**, 195156 (2022).
- [24] J. K. Freericks, V. M. Turkowski, and V. Zlatić, “Nonequilibrium dynamical mean-field theory,” *Phys. Rev. Lett.* **97**, 266408 (2006).
- [25] J. K. Freericks, “Nonequilibrium dynamical mean-field theory,” *Phys. Rev. B* **77**, 075109 (2008).
- [26] H. Aoki, N. Tsuji, M. Eckstein, M. Kollar, T. Oka, and P. Werner, “Nonequilibrium dynamical mean-field theory and its applications,” *Rev. Mod. Phys.* **86**, 779–837 (2014).
- [27] J. K. Freericks and A. V. Joura, “Nonequilibrium dynamical mean-field theory,” in *Electron Transport in Nanosystems*, edited by J. Bonča and S. Kruchinin, NATO Science for Peace and Security Series B: Physics and Biophysics (Springer, Dordrecht, 2008), pp. 219–236, doi:10.1007/978-1-4020-9146-9.
- [28] A. V. Joura, J. K. Freericks, and Th. Pruschke, “Correlated electron transport through mesoscopic structures,” *Phys. Rev. Lett.* **101**, 196401 (2008).
- [29] N. Tsuji, T. Oka, and H. Aoki, “Nonequilibrium steady state of photoexcited correlated electrons in the presence of dissipation,” *Phys. Rev. B* **78**, 235124 (2008).
- [30] H. F. Fotso and J. K. Freericks, “Nonequilibrium dynamical mean-field theory for strongly correlated materials,” *Front. Phys.* **8**, 324 (2020).
- [31] H. F. Fotso, K. Mikelsons, and J. K. Freericks, “Nonequilibrium dynamics of strongly correlated electrons under a uniform electric field,” *Sci. Rep.* **4**, 4699 (2014).
- [32] Y. Zhu, L. Liu, and H. Guo, “Quantum transport theory with nonequilibrium coherent potentials,” *Phys. Rev. B* **88**, 205415 (2013).
- [33] A. V. Kalitsov, M. G. Chshiev, and J. P. Velez, “Nonequilibrium coherent potential approximation for electron transport,” *Phys. Rev. B* **85**, 235111 (2012).
- [34] P. Soven, “Coherent-potential model of substitutional disordered alloys,” *Phys. Rev.* **156**, 809–813 (1967).
- [35] S. Kirkpatrick, B. Velický, and H. Ehrenreich, “Paramagnetic Ni–Cu alloys: Electronic density of states in the coherent-potential approximation,” *Phys. Rev. B* **1**, 3250–3256 (1970).
- [36] B. Velický, “Theory of electronic transport in disordered binary alloys: Coherent-potential approximation,” *Phys. Rev.* **184**, 614–627 (1969).

- [37] F. Yonezawa and K. Morigaki, “Coherent potential approximation: Basic concepts and applications,” *Prog. Theor. Phys. Suppl.* **53**, 1–76 (1973).
- [38] L. V. Keldysh, “Diagram technique for nonequilibrium processes,” *Zh. Eksp. Teor. Fiz.* **47**, 1945–1957 (1964) [*Sov. Phys. JETP* **20**, 1018–1026 (1965)].
- [39] G. Stefanucci and R. van Leeuwen, *Nonequilibrium Many-Body Theory of Quantum Systems: A Modern Introduction* (Cambridge University Press, Cambridge, 2013), doi:10.1017/CBO9781139023979.
- [40] J. Rammer, *Quantum Field Theory of Nonequilibrium States* (Cambridge University Press, Cambridge, 2007), doi:10.1017/CBO9780511618956.
- [41] L. P. Kadanoff and G. Baym, *Quantum Statistical Mechanics* (Benjamin, New York, 1962), doi:10.1201/9780429493218.
- [42] J. Rammer, *Quantum Field Theory of Non-Equilibrium States* (Cambridge University Press, Cambridge, 2007), doi:10.1017/CBO9780511618956.
- [43] G. Stefanucci and R. van Leeuwen, *Nonequilibrium Many-Body Theory of Quantum Systems: A Modern Introduction* (Cambridge University Press, Cambridge, 2025), doi:10.1017/9781009536776.
- [44] A. Kamenev, *Field Theory of Non-Equilibrium Systems* (Cambridge University Press, Cambridge, 2011), doi:10.1017/CBO9781139003667.
- [45] M. Eckstein, M. Kollar, and P. Werner, “Interaction quench in the Hubbard model: Relaxation of the spectral function and the optical conductivity,” *Phys. Rev. B* **81**, 115131 (2010).